

# Universal manuscript template for Optica Publishing Group journals

## 1. Abstract

2 Lorem ipsum ~ 100 words

## 3 2. Introduction

4 IR spectroscopy has seen significant interest and application in bio-imaging because it provides a  
5 chemical fingerprint of underlying samples in a label-free way [1]. However, although the most  
6 relevant chemical information can be gathered in the mid-infrared ( $\sim 3 - 12 \mu\text{m}$ ), slow signal  
7 acquisition is often a limiting factor, whose trade-off can keep it from competing with label-based  
8 fluorescence microscopy.

9 Fig. 1 attempts to visualize the significant developments that have been made in mid-infrared  
10 hyperspectral imaging over roughly the last two decades. Experiments are mapped onto the  
11 two important metrics of spectra acquisition speed, which captures the rate at which spectra  
12 are gathered, and optical bandwidth, which captures the breadth of chemical content that can  
13 be observed. The two variables are plotted against each other, since a significant difficulty lies  
14 in achieving both metrics simultaneously. For a better one to one comparison, the acquisition  
15 speeds listed for experiments that use focal plane arrays have been normalized to that of an  
16 analogous point scanning experiment.  
17

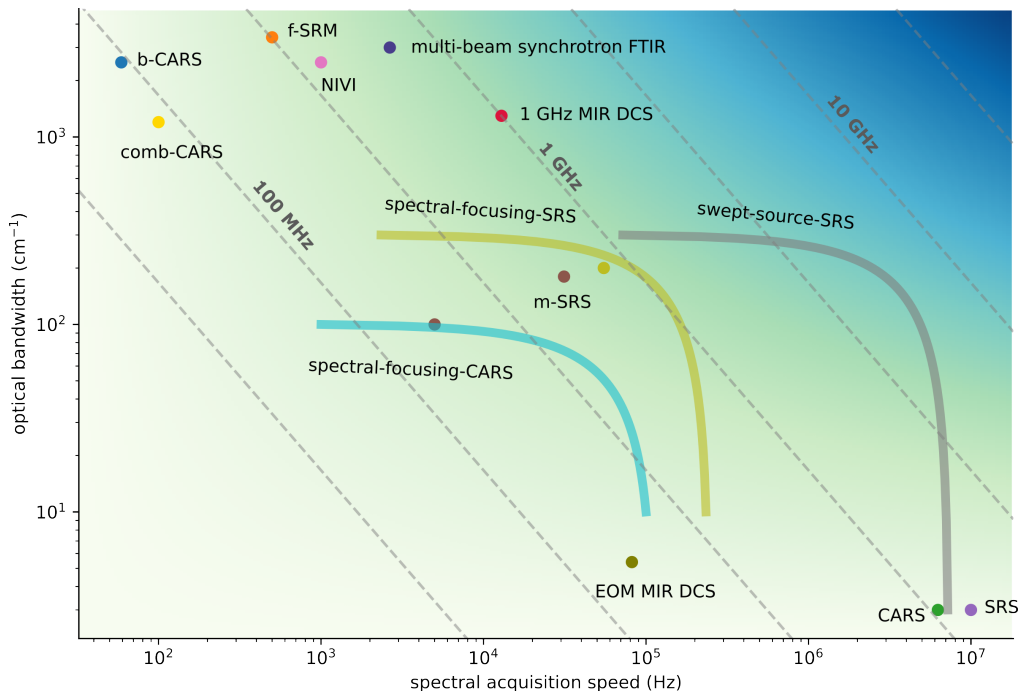


Fig. 1. Performance map of mid-infrared hyperspectral imaging. Broadband CARS (b-CARS) [2], femtosecond Stimulated Raman Microscopy (f-SRM) [3], in-vivo video rate CARS [4], in-vivo video rate SRS [5], multiplexed SRS (m-SRS) [6, 7], nonlinear interferometric vibrational imaging (NIVI) [8], swept-source SRS [9], spectral-focusing SRS [10], spectral-focusing CARS [11], spectral-focusing SRS [12], comb-CARS [13], multi-beam synchrotron FTIR [14], electro-optic modulator comb MIR DCS [15]

19 A few of the most notable experiments have utilized coherent Raman spectro-imaging, where  
 20 in-vivo video-rate speeds have been demonstrated in the mid-infrared [4, 5]. Whereas initial  
 21 demonstrations were over a narrow bandwidth ( $\sim 3 \text{ cm}^{-1}$ ), broad bandwidths at high acquisition  
 22 speeds have been demonstrated using rapidly rotating polygonal mirror scanners [12, 16]. However,  
 23 the stated metrics are only possible with the strong Raman absorption cross-sections around  
 24  $2900 \text{ cm}^{-1}$ , which precludes Raman spectroscopy-based platforms from achieving the same  
 25 performance in the fingerprint region at longer wavelengths.

26 Conversely, Fourier transform spectroscopy (FTS) and quantum cascade laser (QCL) based  
 27 imaging are attractive due to their broad applicability across the mid to long wavelength infrared.  
 28 The high absorption cross-sections can also alleviate the need for operation at powers close to  
 29 sample-damage thresholds, a concern that is applicable to biological samples. In this category,  
 30 FTS spectrometers coupled to broadband and bright sources such as synchrotron facilities have  
 31 set the state of the art for the combination of spectral bandwidth and speed [14]. The coupling of  
 32 broadband synchrotron light into a microscope requires the active stabilization of a beam bundle.  
 33 However, a widely accessible imaging method would benefit from having a simple and table  
 34 top setup. QCL lasers are attractive due to their direct emission in the mid-infrared and small  
 35 footprint, although their performance is best leveraged in narrowband applications. Tunable QCL  
 36 packages consisting of multiple QCL chips combined into one device [17] can nominally reach  
 37 broad spectral coverage, but struggle to reach noise figures comparable to platforms based on  
 38 mode-locked lasers.

More recently, dual-comb spectroscopy (DCS) in the frequency comb community has become  
 a popular platform, due to its improved stability and speed when compared to classical FTS [18].  
 In this modality, the interference of two frequency combs maps a Nyquist band from the optical  
 domain down into the RF. One of the most important considerations in DCS is the direct trade-off  
 between the frequency resolution/repetition rate  $f_r$  and the size of the optical Nyquist window  
 $\Delta\nu$ :

$$\Delta\nu = \frac{f_r^2}{2\Delta f_r} \quad (1)$$

39 where  $\Delta f_r$  is the interferogram acquisition rate equal to the difference of the two laser repetition  
 40 rates. The diagonal dashed lines in Fig. 1., show the  $f_r^2/2$  trade-off between resolvable bandwidth  
 41 and acquisition speed in DCS for different repetition rates. Evidently, when broad absorption  
 42 features allow for coarse resolution, the highest repetition rates are desired. However, in order  
 43 to reach sufficient power per comb tooth, in practice the pulse energy required for nonlinear  
 44 frequency down-conversion from the near-infrared sets an upper limit on the obtainable repetition  
 45 rate. In this work, we utilize a set of recently developed 1-GHz mid-infrared frequency combs [19]  
 46 to integrate a dual-comb spectrometer with a confocal microscope. We capitalize on the high  
 47 repetition rate by fully filling the third Nyquist band ( $2595\text{cm}^{-1}$ – $3890\text{cm}^{-1}$  at  $\Delta f_r = 12.86\text{kHz}$ ).  
 48 The system is among the fastest performers in the class of spectrometers covering over 1000  
 49  $\text{cm}^{-1}$  with high spectral resolution in the mid-infrared.

50 However, pointing to the dashed line in the upper right corner of Fig. 1, in order to achieve the  
 51 ultimate goal of label-free broadband video-rate imaging, we note that the ideal DCS platform  
 52 would operate with repetition rates of 10 GHz or higher. Such systems would likely require either  
 53 high-power amplifiers or a nanophotonic design capable of generating equivalent bandwidths in  
 54 the mid-infrared with pump pulse energies around 100 pJ.

### 55 3. Experiment

56 With long-term stability in mind, a single-branch intra-pulse difference frequency generation  
 57 (DFG) design is used to generate light in the mid-infrared [19]. Shown in Fig. 2, to compensate  
 58 for the low conversion efficiency of the single-branch design, octave spanning few cycle NIR

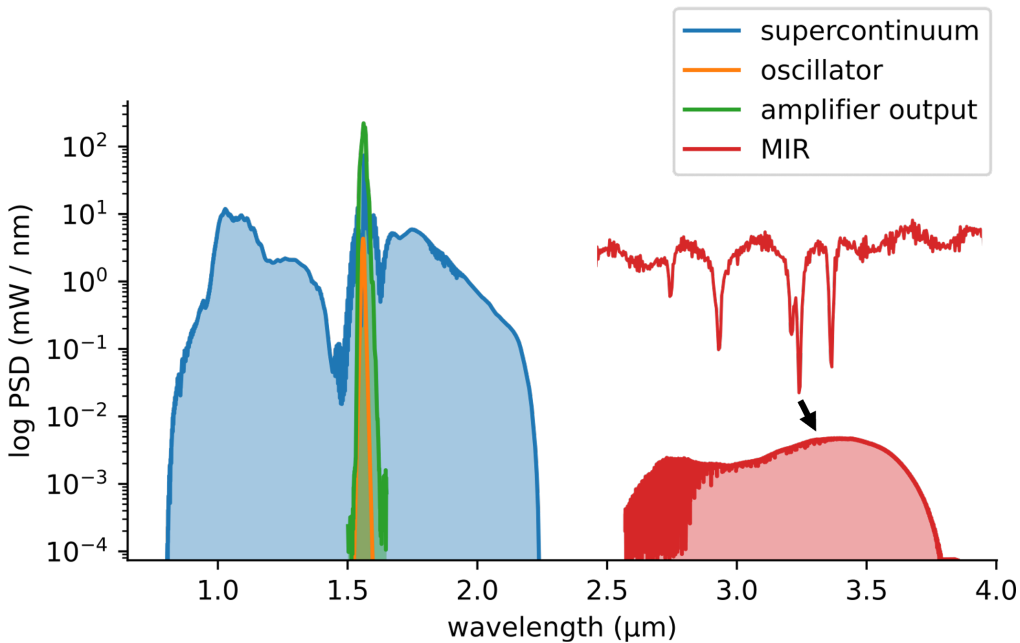


Fig. 2. 1 GHz MIR Frequency Comb. The spectral evolution through successive stages of the system: oscillator → chirped-pulse amplifier → few-cycle supercontinuum generation → MIR frequency down conversion. The inset shows a zoom in of waterlines that are resolved when using the full 1 GHz frequency resolution.

59 pulses generated via soliton self-compression in anomalous dispersion highly nonlinear fiber are  
 60 used to drive the nonlinear frequency down conversion to the mid-infrared. Although coverage  
 61 of the 6-12  $\mu\text{m}$  wavelength region can be achieved for one laser system, due to the lack of  
 62 nonlinear crystals in this work more widely available lithium niobate is used to cover the 3 - 5  
 63  $\mu\text{m}$  wavelength window.

64 Two 1-GHz mid-infrared frequency combs are generated and coupled into  $\text{InF}_3$  single-mode  
 65 fiber for delivery to the experiment. The output beam is collimated with a two inch off-axis  
 66 parabolic mirror, and a reflective confocal microscope with 0.58 NA is used to image the beam  
 67 onto a glass slide ( $\sim 3.8 \mu\text{m}$  pixel size). A set of linear translation stages are used to raster scan  
 68 the sample. The data is acquired via trigger, with the trigger spacing and scan speed set by the  
 69 desired spatial sampling interval. The scan speed is limited by the interferogram acquisition time,  
 70 which is fundamentally set by the repetition rate of the laser. The transmitted signal is focused  
 71 onto a high-speed MCT detector, whose AC coupled port is digitized at 1 GS/s using an FPGA.  
 72 The data is streamed concurrently from the card memory into PC RAM for real-time analysis,  
 73 and such that the card-memory does not limit the data volume. Owing to the fairly high 500  
 74 MHz Nyquist frequency, and the placement of all fiber amplifiers in loop for the phase-locks  
 75 of the two frequency combs, over one thousand interferograms can be directly averaged before  
 76 phase correction needs to be employed.

#### 77 4. Results

78 As a demonstration, hyperspectral images are taken of a USAF resolution target composed of  
 79 SU-8 photoresist patterned onto a 500  $\mu\text{m}$  thick Silicon wafer. Five hundred spectra are averaged  
 80 at each pixel and apodized to 100 GHz ( $3.3 \text{ cm}^{-1}$ ). The images are generated by integrating a  
 81  $63\text{cm}^{-1}$  window around the peak absorption at  $2930\text{cm}^{-1}$  using the peak absorbance value at

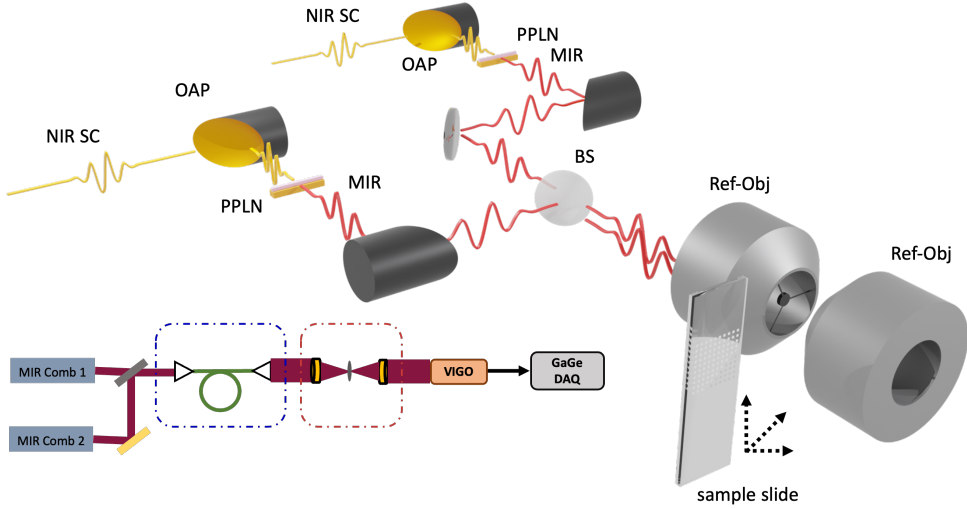


Fig. 3. Experimental Setup. Two mid-infrared frequency combs generated through intra-pulse difference frequency generation are passed collinearly through a confocal microscope. Hyperspectral images are collected by raster scanning the sample slide. The transmitted signal is collected and digitized in a high-speed MCT mid-infrared detector and FPGA.

82 The broad absorption of SU-8 is shown in Fig. 4. (b),, with the images

### 83 5. DCS Imaging Speed

Regardless of the imaging method, the final determination of imaging speed is given by the time needed to reach sufficient SNR at each pixel. Specifically for DCS microscopy, the target SNR and frequency resolution sets the pixel dwell time. In DCS, the absorbance noise  $\sigma$  scales with the frequency resolution and number of averaged spectra  $N_{avg}$  according to [20]:

$$\sigma \propto \frac{N}{\sqrt{N_{avg}}} \quad (2)$$

84 where  $N$  is the number of frequency bins. This scaling rule is shown in Fig. 6. (c-d),, where it  
 85 is observed to match the experimentally measured absorbance noise. The two-variable map in  
 86 Fig. 6. (d). should apply more generally to to any DCS point scanning microscopy, but with the  
 87 time axis scaled accordingly to the repetition rate.

88 Shown in Fig. 6. (a),, a baseline for 1 GHz DCS is that a  $1000 \text{ cm}^{-1}$  Nyquist window can be  
 89 covered with  $\sim 17 \text{ kHz}$  spectra acquisition speed, which is a two order magnitude improvement  
 90 over well established 100 MHz mid-infrared dual-comb systems. In Fig. 6. (b),, a single-shot  
 91 spectrum ( $77 \mu\text{s}$ ) at 1-GHz has low signal to noise, but can be averaged to high SNR in two  
 92 seconds ( $>25,000$  spectra). However, a high SNR can be achieved in  $\sim 39 \text{ ms}$  at 500 averages if  
 93 the interferograms are apodized to 100 GHz ( $\sim 3.33 \text{ cm}^{-1}$ ). The SNR as a function of averaging  
 94 time and frequency resolution is shown in Fig. 6. (c-d); the absorbance noise always averages  
 95 down according to  $1/\sqrt{N_{avg}}$ , but with coarser resolution resulting in a directly proportional  
 96 overall noise reduction.

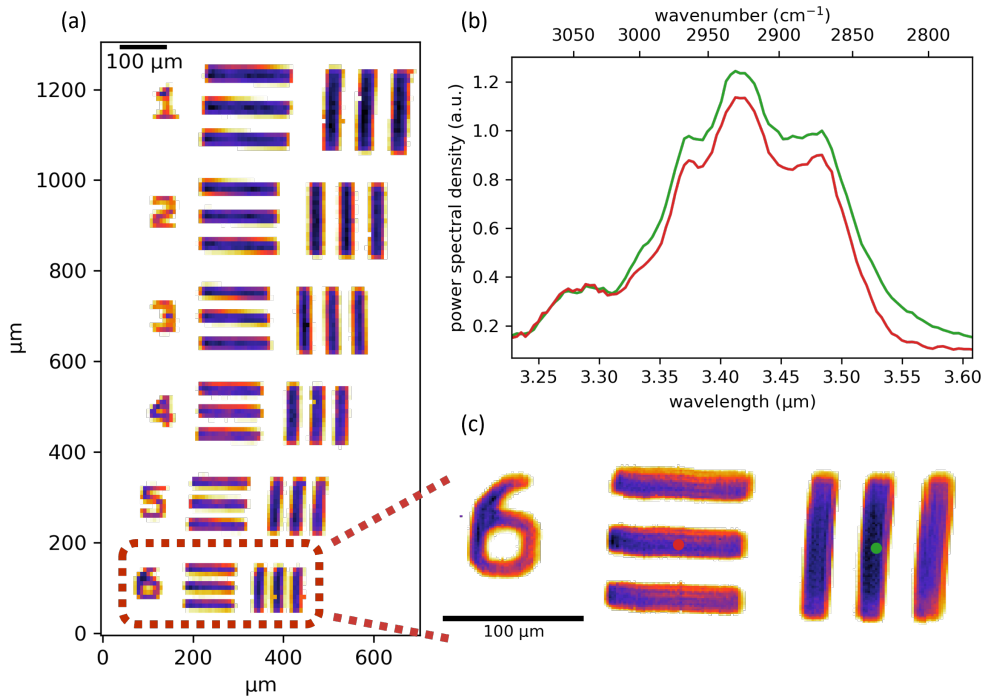


Fig. 4. Caption

## 97 References

- 98 1. M. J. Baker, J. Trevisan, P. Bassan, R. Bhargava, H. J. Butler, K. M. Dorling, P. R. Fielden, S. W. Fogarty, N. J.  
99 Fullwood, K. A. Heys, C. Hughes, P. Lasch, P. L. Martin-Hirsch, B. Obinaju, G. D. Sockalingum, J. Sulé-Suso, R. J.  
100 Strong, M. J. Walsh, B. R. Wood, P. Gardner, and F. L. Martin, "Using Fourier transform IR spectroscopy to analyze  
101 biological materials," *Nat. Protoc.* **9**, 1771–1791 (2014).
- 102 2. T. W. Kee and M. T. Cicerone, "Simple approach to one-laser, broadband coherent anti-Stokes Raman scattering  
103 microscopy," *Opt. Lett.* **29**, 2701 (2004).
- 104 3. E. Ploetz, S. Laimgruber, S. Berner, W. Zinth, and P. Gilch, "Femtosecond stimulated Raman microscopy," *Appl.  
105 Phys. B* **87**, 389–393 (2007).
- 106 4. C. L. Evans, E. O. Potma, M. Puoris'haag, D. Côté, C. P. Lin, and X. S. Xie, "Chemical imaging of tissue *in vivo* with  
107 video-rate coherent anti-Stokes Raman scattering microscopy," *Proc. National Acad. Sci.* **102**, 16807–16812 (2005).
- 108 5. B. G. Saar, C. W. Freudiger, J. Reichman, C. M. Stanley, G. R. Holtom, and X. S. Xie, "Video-Rate Molecular  
109 Imaging in Vivo with Stimulated Raman Scattering," *Science* **330**, 1368–1370 (2010).
- 110 6. D. Fu, F.-K. Lu, X. Zhang, C. Freudiger, D. R. Pernik, G. Holtom, and X. S. Xie, "Quantitative Chemical Imaging  
111 with Multiplex Stimulated Raman Scattering Microscopy," *J. Am. Chem. Soc.* **134**, 3623–3626 (2012).
- 112 7. C.-S. Liao, M. N. Slipchenko, P. Wang, J. Li, S.-Y. Lee, R. A. Oglesbee, and J.-X. Cheng, "Microsecond scale  
113 vibrational spectroscopic imaging by multiplex stimulated Raman scattering microscopy," *Light. Sci. & Appl.* **4**,  
114 e265–e265 (2015).
- 115 8. P. D. Chowdary, Z. Jiang, E. J. Chaney, W. A. Benalcazar, D. L. Marks, M. Gruebele, and S. A. Boppart, "Molecular  
116 Histopathology by Spectrally Reconstructed Nonlinear Interferometric Vibrational Imaging," *Cancer Res.* **70**,  
117 9562–9569 (2010).
- 118 9. Y. Ozeki, W. Umemura, Y. Otsuka, S. Satoh, H. Hashimoto, K. Sumimura, N. Nishizawa, K. Fukui, and K. Itoh,  
119 "High-speed molecular spectral imaging of tissue with stimulated Raman scattering," *Nat. Photonics* **6**, 845–851  
120 (2012).
- 121 10. D. Fu, G. Holtom, C. Freudiger, X. Zhang, and X. S. Xie, "Hyperspectral Imaging with Stimulated Raman Scattering  
122 by Chirped Femtosecond Lasers," *The J. Phys. Chem. B* **117**, 4634–4640 (2013).
- 123 11. C. Di Napoli, I. Pope, F. Masia, P. Watson, W. Langbein, and P. Borri, "Hyperspectral and differential CARS  
124 microscopy for quantitative chemical imaging in human adipocytes," *Biomed. Opt. Express* **5**, 1378 (2014).
- 125 12. H. Lin, H. J. Lee, N. Tague, J.-B. Lugagne, C. Zong, F. Deng, J. Shin, L. Tian, W. Wong, M. J. Dunlop, and J.-X.  
126 Cheng, "Microsecond fingerprint stimulated Raman spectroscopic imaging by ultrafast tuning and spatial-spectral

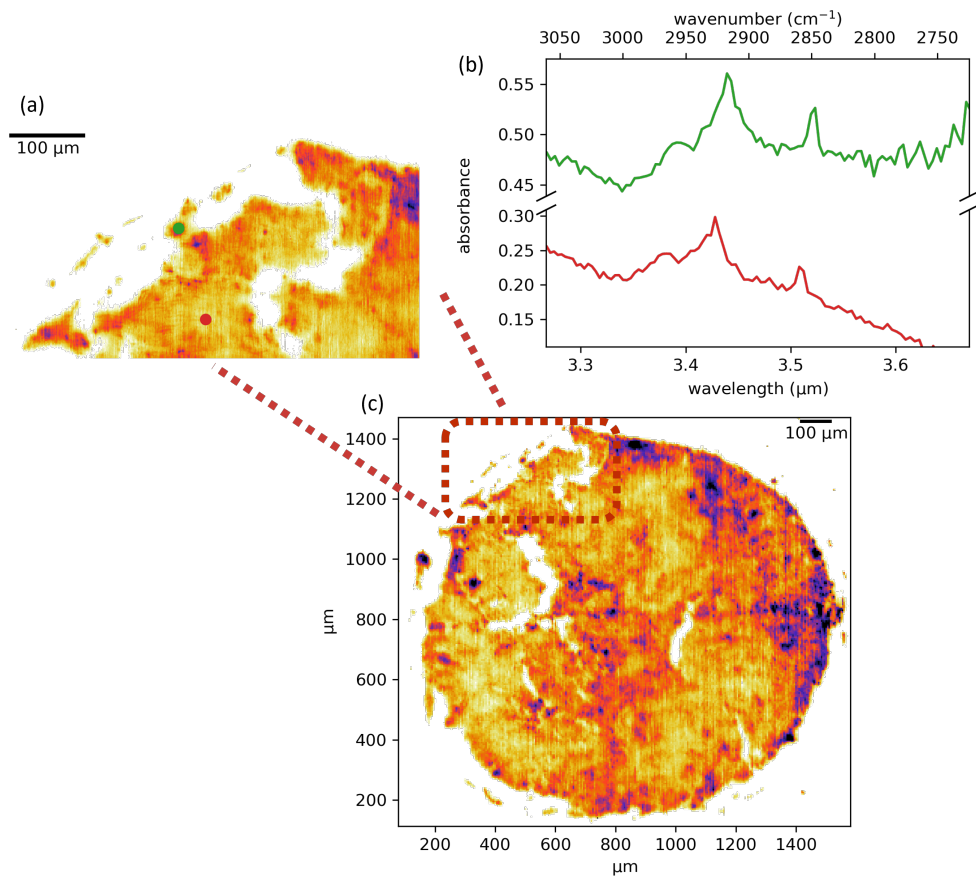


Fig. 5. Caption

- learning,” Nat. Commun. **12**, 3052 (2021).
- 127  
128 13. T. Ideguchi, S. Holzner, B. Bernhardt, G. Guelachvili, N. Picqué, and T. W. Hänsch, “Coherent Raman spectro-imaging  
129 with laser frequency combs,” Nature **502**, 355–358 (2013).
- 130 14. M. J. Nasse, M. J. Walsh, E. C. Mattson, R. Reininger, A. Kajdacsy-Balla, V. Macias, R. Bhargava, and C. J.  
131 Hirschmugl, “High-resolution Fourier-transform infrared chemical imaging with multiple synchrotron beams,” Nat.  
132 Methods **8**, 413–416 (2011).
- 133 15. F. Ullah Khan, G. Guarnizo, and P. Martín-Mateos, “Direct hyperspectral dual-comb gas imaging in the mid-infrared,”  
134 Opt. Lett. **45**, 5335 (2020).
- 135 16. M. Tamamitsu, Y. Sakaki, T. Nakamura, G. K. Podagatlapalli, T. Ideguchi, and K. Goda, “Ultrafast broadband  
136 Fourier-transform CARS spectroscopy at 50,000 spectra/s enabled by a scanning Fourier-domain delay line,” Vib.  
137 Spectrosc. **91**, 163–169 (2017).
- 138 17. K. Yeh, S. Kenkel, J.-N. Liu, and R. Bhargava, “Fast Infrared Chemical Imaging with a Quantum Cascade Laser,”  
139 Anal. Chem. **87**, 485–493 (2015).
- 140 18. I. Coddington, N. Newbury, and W. Swann, “Dual-comb spectroscopy,” Optica **3**, 414 (2016).
- 141 19. N. Hoghooghi, S. Xing, P. Chang, D. Lesko, A. Lind, G. Rieker, and S. Diddams, “Broadband 1-GHz mid-infrared  
142 frequency comb,” Light. Sci. & Appl. **11**, 264 (2022).
- 143 20. N. R. Newbury, I. Coddington, and W. Swann, “Sensitivity of coherent dual-comb spectroscopy,” Opt. Express **18**,  
144 7929 (2010).

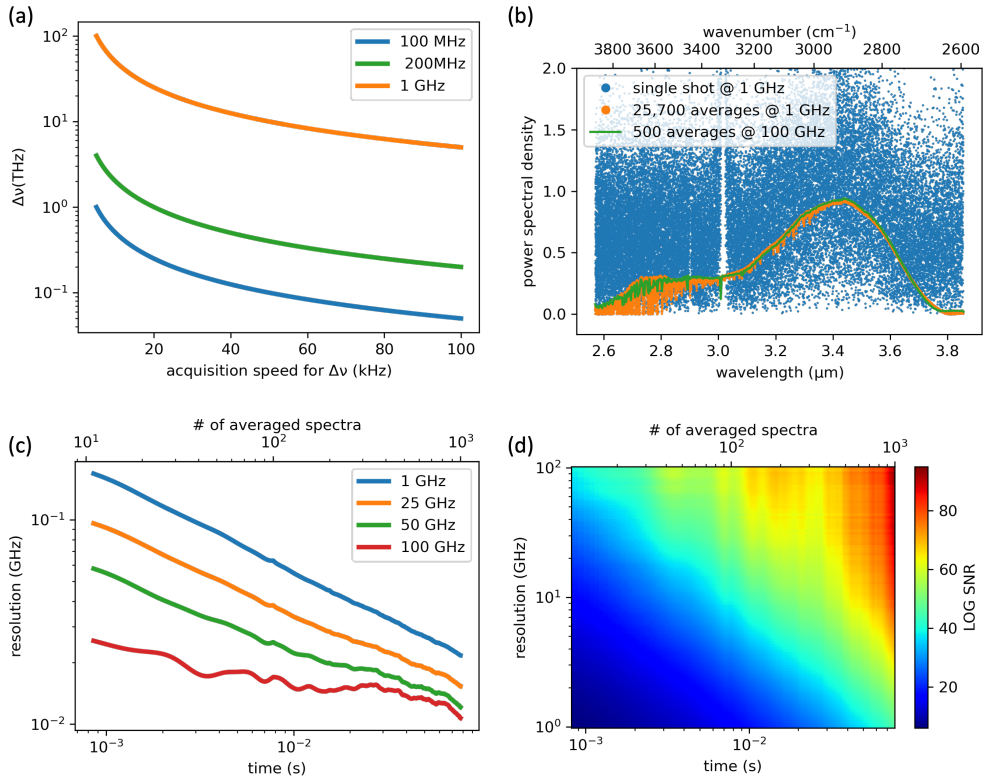


Fig. 6. Summary of DCS Imaging Speed. (a) The size of the optical Nyquist window plotted against acquisition speed ( $\Delta f_r$ ) for different repetition rates. (b) DCS spectrum taken at different averaging times and frequency resolution/apodization windows. (c) The spectra's SNR follow the scaling of Eq. 2, with an example of the 2D parameter space (d) mapped out for the 1-GHz system.